Migration mechanisms and diffusion barriers of vacancies in Ga_{2}O_{3}

Alexandros Kyrtsos, Masahiko Matsubara, and Enrico Bellotti

Phys. Rev. B **95**, 245202 — Published 1 June 2017

DOI: 10.1103/PhysRevB.95.245202

Migration mechanisms and diffusion barriers of vacancies in Ga_2O_3

Alexandros Kyrtsos,[1] Masahiko Matsubara,[1] and Enrico Bellotti[1,2]

[1] *Department of Electrical and Computer Engineering, Boston University, Boston, Massachusetts 02215, USA**

[2] *Division of Materials Science and Engineering, Boston University, Boston, Massachusetts 02215, USA*

We employ the nudged elastic band and the dimer methods within the standard density functional theory (DFT) formalism to study the migration of the oxygen and gallium vacancies in the monoclinic structure of β-Ga_2O_3. We identify all the first nearest neighbor paths and calculate the migration barriers for the diffusion of the oxygen and gallium vacancies. We also identify the metastable sites of the gallium vacancies which are critical for the diffusion of the gallium atoms. The migration barriers for the diffusion of the gallium vacancies are lower than the migration barriers for oxygen vacancies by 1 eV on average, suggesting that the gallium vacancies are mobile at lower temperatures. Using the calculated migration barriers we estimate the annealing temperature of these defects within the harmonic transition state theory formalism, finding excellent agreement with the observed experimental annealing temperatures. Finally, we suggest the existence of percolation paths which enable the migration of the species without utilizing all the migration paths of the crystal.

I. INTRODUCTION

Ga_2O_3 crystallizes in five different phases, conventionally referred to as α, β, γ, δ, and ε. The monoclinic β-Ga_2O_3 is the most stable phase[1] and we will refer to this phase hereinafter.Ga_2O_3 is a promising material for a number of applications. It is already being used as the sensing material in gas sensors due to its resistivity dependence on the concentration of certain gases such as oxygen and hydrogen.[2–4] It exhibits remarkable performance as a gas detector even at temperatures above 900 °C. In addition to its gas sensing applications, this material has attracted a lot of interest for applications as an ultra wide band gap semiconductor. With a band gap of 4.9 eV,[5] it is suitable for optoelectronic applications as a deep UV transparent conducting oxide (TCO).[5,6] TCOs are functional materials which conduct electricity while being transparent in the visible spectrum due to their wide band gap. As a result they are mainly used as transparent electrodes for solar cells, flat panel displays, and light emitting diodes.[7,8]

The basic properties of Ga_2O_3 are known and verified both theoretically and experimentally. It belongs to the monoclinic system (space group $C2/m$) with lattice parameters $a = 12.23$ Å, $b = 3.04$ Å, $c = 5.80$ Å, and an angle $\beta = 103.73°$ between a and c.[9,10] Angle resolved photoemission spectroscopy (ARPES) and first principles calculations agree that Ga_2O_3 is an indirect semiconductor with the conduction band minimum located at the Γ point and the top of the valence band located near the M $= \left(\frac{1}{2}, \frac{1}{2}, \frac{1}{2}\right)$ point.[11–13] However, the energy difference between the actual valence band maximum and the Γ point of the valence band is only a few meV which makes Ga_2O_3 a Γ direct band gap material for all practical purposes. Relevant technological applications require the precise control of the conductivity of the material. Ga_2O_3 exhibits unintentional n-type conductivity as many other TCOs.[8] The conductivity of Ga_2O_3 is an easily tunable property over many orders of magnitude (10^{-12}–$10^{2}\,\Omega^{-1}\mathrm{cm}^{-1}$) using the appropriate dopants and growth conditions.[6,14–16] So far, p-type conductivity has been observed only in Ga_2O_3 nanowires doped with nitrogen or zinc.[17,18] Another property that is often overlooked is the anisotropy of the band gap depending on the polarization of the incident light. Typical values of the band gap range from 4.5 to 4.9 eV depending on the polarization of the light with respect to the b and c axis of the crystal.[19–21]

The luminescence of Ga_2O_3 has been studied extensively in the past and can be summarized as follows. Depending on the sample preparation and the dopant, it can exhibit UV, blue, and green emissions and the origin of each band has been discussed previously.[22] The UV emission is generally impurity independent and it is attributed to the recombination of free electrons and self-trapped holes (STHs).[23] Oxygen vacancies have also been reported to play a role in UV emission.[24] The blue luminescence is attributed to dopants such as Zr and Si as well as oxygen vacancies in as-grown samples.[22,25] The green luminescence is present only with certain impurities such as Be, Ge, and Sn but there is no definitive answer on the nature of this emission yet.[22,26]

Point defects are unavoidable and they can be introduced to the material either during the fabrication or afterward through various ways such as doping and radiation damage. Oxygen vacancies have traditionally been held responsible for causing the unintentional n-type conductivity of Ga_2O_3.[6,24,27] On the other hand, gallium vacancies act as compensating acceptors, decreasing the conductivity.[28] Hence, studying the intrinsic point defects is important for determining the electrical and optical properties of Ga_2O_3. Previous theoretical studies have investigated the electronic, thermodynamic, and structural properties of Ga_2O_3.[1,11,12,28–35] The tools for these studies vary from empirical interatomic potentials to density functional theory (DFT) using standard and hybrid functionals. The results show that oxygen and gallium vacancies have low formation energies and intro-

duce deep donor and acceptor states respectively. Other common impurities include Si and H. In particular, the complexes of hydrogen with gallium vacancies exhibit low formation energies.[28] Apart from the work of Blanco *et al.*[35] who used empirical interatomic potentials to determine the energetics and migration of point defects in Ga_2O_3, a comprehensive study of the kinetics of the defects is still missing.

It is the aim of this paper to serve as a comprehensive study of the migration barriers and the migration paths of oxygen and gallium vacancies in Ga_2O_3 using first principles calculations. We consider the complete set of migration paths to first nearest neighbors in the monoclinic structure of Ga_2O_3 and we propose the most probable mechanisms for the migration of both gallium and oxygen vacancies. In addition to the migration barriers of the vacancies, which are the main scope of this paper, we also investigate their formation energies and we include the metastable sites of the gallium vacancies which are essential for studying the kinetics of these defects.

The manuscript is organized as follows. First, in Sec. II we discuss the methods we used and the computational details of our calculations. In Sec. III we discuss the migration paths in Ga_2O_3 and we present the results of our calculations for the formation energies and the migration barriers of the gallium and oxygen vacancies. In Sec. IV we discuss potential implications of our results and Sec. V summarizes and concludes the manuscript.

II. METHOD

We employ DFT[36,37] calculations using the the projector augmented wave (PAW)[38,39] method as implemented in the Vienna *Ab-initio* Simulation Package (VASP).[40] The exchange-correlation energy is calculated using the generalized gradient approximation (GGA) in the parametrization by Perdew, Burke, and Ernzerhof (PBE).[41] For the calculation of the migration barriers and the investigation of the minimum energy paths (MEP) we employ the nudged elastic band (NEB)[42–44] and dimer[45] methods as implemented in VASP through the VTST-Tools by Henkelman, Jónsson and others.[46]

The plane-wave basis cutoff energy was set at 450 eV for all our calculations. The $3d$ electrons of Gallium were treated as valence electrons and all the calculations were spin polarized. The obtained crystallographic parameters in our calculations are $a = 12.469$ Å, $b = 3.088$ Å, $c = 5.882$ Å and $\beta = 103.7°$ which are in excellent agreement with previously calculated results[1,29] and in good agreement with the experimental values.[9,10,47] Fig. 1 shows the 120-atom supercell as well as the 20-atom unit cell of the crystal with the corresponding crystallographic directions. Our calculated band gap of 2.0 eV severely underestimates the experimental band gap of 4.9 eV. This was expected since calculations using the local density approximation (LDA) or GGA are known for underestimating the band gap.

The convergence of the formation energies and the migration barriers was verified using supercells of different sizes. We used supercells of 120, 160, 200, 240, 300, and 360 atoms. The sampling of the Brillouin zone was done using a $2\times2\times2$ Monkhorst-Pack mesh which results in 4 irreducible k-points. The atomic configurations of the initial states were optimized using a force criterion of 5×10^{-3} eV/Å. In the case of the NEB and the dimer calculations, the images were relaxed with a force criterion of 10^{-2} eV/Å.

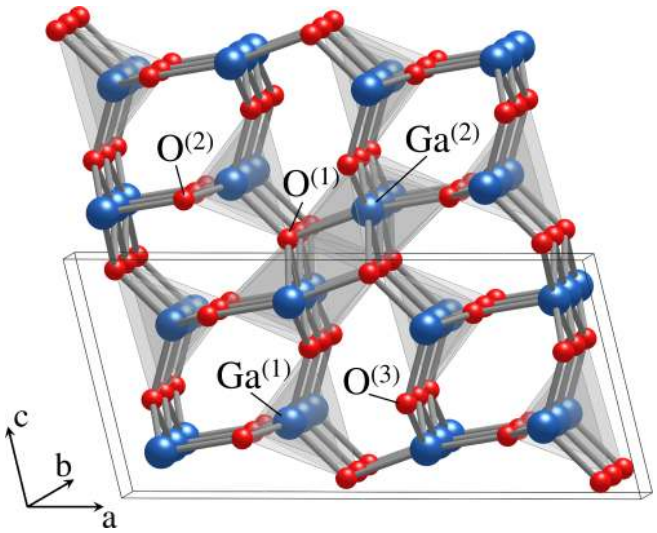

FIG. 1. The 120-atom supercell showing the monoclinic ($C2/m$) crystal structure and the unit cell of β-Ga_2O_3. There are two different gallium and three different oxygen sites designated as $Ga^{(1)}$, $Ga^{(2)}$ and $O^{(1)}$, $O^{(2)}$, and $O^{(3)}$ respectively.

The formation energy of a defect in charge state q is calculated using the well established formula[48]

$$E_{\mathrm{f}}^{q} = E_{\mathrm{tot}}^{\mathrm{def}} - E_{\mathrm{tot}}^{\mathrm{bulk}} - \sum_i n_i\mu_i + q\,(E_{\mathrm{F}} + E_{\mathrm{VBM}}) + Q_{\mathrm{c}}, \quad (1)$$

where $E_{\mathrm{tot}}^{\mathrm{def}}$ is the total energy of the supercell including the defect and $E_{\mathrm{tot}}^{\mathrm{bulk}}$ is the total energy of the bulk supercell. μ_i indicates the chemical potential of the species i added ($n_i > 0$) or removed ($n_i < 0$) for the creation of the defect. The Fermi energy, E_{F}, is referenced at the valence band maximum in the bulk such that $E_{\mathrm{F}} \geq 0$. Due to this choice of reference the energy of the valence band maximum in the bulk, E_{VBM}, needs to be taken into account explicitly. Finally, the term Q_{c} accounts for the electrostatic corrections that are necessary to be taken into account due to the long range electrostatic interaction of the charged defects of the neighboring supercells.

Treating the Fermi energy in Eq. (1) as an independent variable, the formation energy of a defect at a given charge state varies linearly with E_{F}. At any given Fermi level, one of the charge states exhibits the lowest formation energy with respect to the others indicating that it is the most favorable. The positions of the Fermi level at

which the lowest energy charge states change are called thermodynamic transition levels or ionization energies. Thus, the thermodynamic transition level, $\epsilon(q_1/q_2)$, between the charge states q_1 and q_2 is defined as

$$\epsilon(q_1/q_2) = \frac{E_{\rm f}^{q_1}|_{E_{\rm F}=0} - E_{\rm f}^{q_2}|_{E_{\rm F}=0}}{q_2 - q_1}, \tag{2}$$

where $E_{\rm f}^{q}|_{E_{\rm F}=0}$ is the formation energy of the defect in charge state q evaluated at $E_{\rm F} = 0$.

For the calculation of the chemical potentials we assume the O_2 molecule and the Ga metal as the limiting phases for the oxygen rich and gallium rich conditions respectively. As a result, $\mu_{\rm O} \leq 1/2 E_{\rm tot}^{\rm O_2}$ and $\mu_{\rm Ga} \leq E_{\rm tot}^{\rm Ga}$ where the equality applies only at oxygen and gallium rich conditions respectively. Additionally, the expression $2\mu_{\rm Ga}+3\mu_{\rm O} = \mu_{\rm Ga_2O_3} = E_{\rm tot}^{\rm Ga_2O_3}$ holds true for the chemical potentials of the species. Hence, the ranges of allowed values for the oxygen and gallium chemical potentials are given as

$$\frac{1}{3}E_{\rm tot}^{\rm Ga_2O_3} - \frac{2}{3}E_{\rm tot}^{\rm Ga} \;\leq\; \mu_{\rm O} \;\leq\; \frac{1}{2}E_{\rm tot}^{\rm O_2} \tag{3}$$

and

$$\frac{1}{2}E_{\rm tot}^{\rm Ga_2O_3} - \frac{3}{4}E_{\rm tot}^{\rm O_2} \;\leq\; \mu_{\rm Ga} \;\leq\; E_{\rm tot}^{\rm Ga}. \tag{4}$$

The supercell approach adopted in our calculations suffers from the electrostatic and elastic interactions of the periodic arrangement of defects in neighboring supercells. Electrostatic interactions are more prominent because of their long range effect. To account for them, we employ the scheme proposed by Freysoldt *et al.*,[49] which corresponds to the correction term $Q_{\rm c}$ in Eq. (1). Electrostatic corrections are crucial for the calculation of the formation energy of a defect even at a low charge state. The migration barrier, $E_{\rm b}$, is defined as the energy difference between the initial state and the saddle point, also known as transition state. In other words, $E_{\rm b} = E_{\rm f}^{\rm s} - E_{\rm f}^{\rm i}$, where $E_{\rm f}^{\rm s}$ is the formation energy of the saddle point and $E_{\rm f}^{\rm i}$ is the formation energy of the initial state. Substituting the formation energies from Eq. (1) leads to the cancellation of most of the terms. The terms that survive are the total energy of the defective supercell, $E_{\rm tot}^{\rm def}$, and the electrostatic correction, $Q_{\rm c}$, for the initial state and the saddle point respectively. As a result, the migration barrier is given as

$$\begin{aligned} E_{\rm b} &= E_{\rm tot}^{\rm s} - E_{\rm tot}^{\rm i} + Q_{\rm c}^{\rm s} - Q_{\rm c}^{\rm i} \\ &= \Delta E_{\rm tot} + \Delta Q_{\rm c}. \end{aligned} \tag{5}$$

The initial state and the saddle point are electronically similar configurations. Hence, it is common to omit the second term in Eq. (5) assuming that the correction term is similar for both the initial state and the saddle point, and thus its effect is negligible. As a result, the migration barrier is determined as the difference of the total energies of the defective supercells in the initial state and the saddle point. In our calculations we explicitly calculated this term for all the migration barriers and we verified that this term is indeed negligible and less than 0.05 eV. In a previous work[50] we have also showed that this term can be omitted. However, it is always a good practice to check whether this term is indeed negligible, especially in defects with high charge states.

Elastic interactions also contribute to the finite supercell error. These interactions can be considered by extrapolating the formation energies to an infinite size supercell based on the known $1/L^3$ scaling for different supercell sizes.[51] The local deformation of the crystal is usually large for the transition states. Hence, the effect of these interactions should be examined for the calculation of migration barriers.

The primary focus of this work is to determine the migration barriers for the diffusion of the vacancies in Ga_2O_3. Hence, an accurate determination of the saddle points for the different paths is necessary. To achieve that we employ the NEB and the dimer methods. The NEB is a chain of states method which is used to trace the MEP using a set of atomic configurations, also known as "images", connecting the initial and final states. In fact, it is used to locate a steepest descent (SD) path from saddle point(s) to minima which in most cases corresponds to the MEP.[52] Additionally, using the climbing image modification (CI-NEB), the forces of the image which is higher in energy are modified so that it is driven to the saddle point. Consequently, the CI-NEB method provides both a good description of the MEP and the configuration of the saddle point. In our NEB calculations we used up to nine images to verify the convergence of the migration barrier versus the number of images and obtain a good description of the migration path. On the other hand, the dimer is a min-mode method relying on a pair of closely separated images to estimate the curvature of the potential energy surface without the need of the costly calculation of the Hessian matrix. The merits and shortcomings of each method have been also discussed in a previous work.[50] Employing both methods provides an efficient approach to determine both the MEP and the saddle point for a given jump.

III. RESULTS

A. Formation energies

Due to the low symmetry of the monoclinic Ga_2O_3 crystal, there are two different Ga and three different O sites. The Ga atoms are either tetrahedrally or octahedrally coordinated with their surrounding oxygen neighbors and we refer to them as $Ga^{(1)}$ and $Ga^{(2)}$ respectively. Similarly we use the notation $O^{(1)}$, $O^{(2)}$, and $O^{(3)}$ for the three different oxygen sites. $O^{(1)}$ refers to the fourfold coordinated oxygen which forms an irregular tetrahedron with its surrounding gallium neighbors. $O^{(2)}$ and $O^{(3)}$ are threefold coordinated. The crystal structure of

Ga_2O_3 with the different gallium and oxygen atoms is shown in Fig. 1. As a result, there are five different vacancies in total. Based on the notation we introduced, we refer to these vacancies as $V_O^{(1-3)}$ and $V_{Ga}^{(1,2)}$ respectively.

LDA and GGA are known for underestimating the band gap. This causes some of the charged states to have delocalized electrons. In other words, electrons that occupy a state in the conduction band instead of localizing in the vicinity of the defect. Checking the localization of the electrons is important while doing calculations of charged defects. All the vacancies related calculations were found to keep the charge localized around the defect even within GGA and the results are qualitatively correct compared to hybrid functional calculations.[29] The situation is different for the interstitials because GGA has proven to be insufficient to predict the correct charge states within the band gap.[29] However, since the interstitial are not part of this work, we will not delve deeper into this matter. Fig. 2 shows the formation energies of the vacancies in oxygen and gallium rich conditions using the 160-atom supercell. Compared to the larger supercells of up to 360 atoms, the 160-atom supercell yields converged results for the formation energies of the vacancies. Gallium vacancies become relevant in O-rich growth conditions and n-type doping. On the other hand, oxygen vacancies exhibit low formation energies both in oxygen and gallium rich conditions. Our results are in excellent agreement with previous theoretical data.[29]

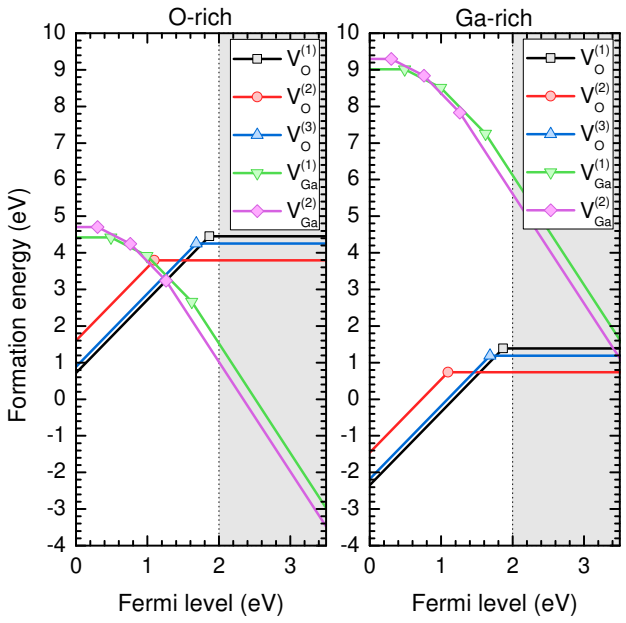

FIG. 2. Formation energies of oxygen and gallium vacancies in oxygen (left) and gallium (right) rich conditions. The dotted vertical line represents the calculated conduction band minimum.

There are four different channels in the b direction of the crystal as shown in Fig. 3. Two of them have the shape of an irregular hexagon. and the difference between them lies in the fact that one of them is surrounded by $O^{(1)}$ and $O^{(2)}$ while the other is surrounded by $O^{(2)}$ and $O^{(3)}$. The other two consist of a rhombic and an eight sided channel. There has been a report[28] of a global minimum for the gallium vacancy which is neither the $V_{Ga}^{(1)}$ nor the $V_{Ga}^{(2)}$. This new site is octahedrally coordinated in the center of one of the hexagonal channels. However, the authors of this work did not specify in which channel this site refers to. Through our migration studies we were able to verify the existence of a minimum in both hexagonal channels. In addition, we identified a third minimum located at the eight sided channel, between $Ga^{(1)}$ and $Ga^{(2)}$. The last is a tetrahedrally coordinated site and we refer to it as $Ga^{(a)}$. We also denote as $Ga^{(b)}$ the site located in the hexagonal channel surrounded by $O^{(1)}$ and $O^{(2)}$. The site at the center of the other hexagonal channel surrounded by $O^{(2)}$ and $O^{(3)}$ is denoted as $Ga^{(c)}$. Fig. 3 shows the positions of these minima. Notice that this figure should be used only as a reference for the positions of the minima and not the real geometries of the surrounding atoms.

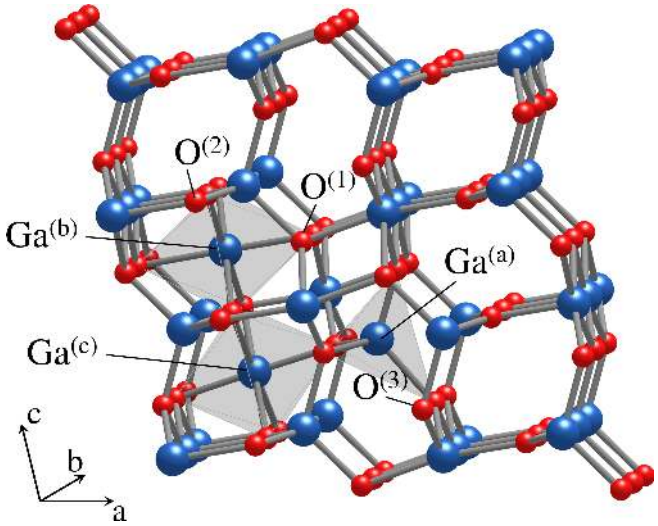

FIG. 3. The 120-atom supercell showing the metastable sites for the gallium vacancies denoted as $Ga^{(a)}$, $Ga^{(b)}$, and $Ga^{(c)}$.

Both the site reported before and the two novel sites we identified in this work are important in the study of the migration paths which we discuss in detail in the following section of the manuscript. We will refer to $Ga^{(a)}$, $Ga^{(b)}$, and $Ga^{(c)}$ as metastable sites even though the term should be used only for sites which exhibit higher formation energy than the stable sites $V_{Ga}^{(1)}$ and $V_{Ga}^{(2)}$.

B. Migration barriers

The low symmetry of the Ga_2O_3 crystal allows for a number of possible paths for the migration of oxygen and gallium vacancies. In fact, there is no clear distinction be-

tween first and second nearest neighbors in the sublattice of each species. By convention, we consider atoms with distance of less than 3.5 Å to be first nearest neighbors and we study the jumps between these sites. Following this convention, we identify 14 different jumps for the migration of V_O and nine different jumps for the migration of V_{Ga}. Including the metastable sites, the number of different jumps increases to 10 for the gallium vacancy. We use the letters p and q to denote jumps of oxygen and gallium vacancies respectively. Fig. 4 shows all the possible first nearest neighbor jumps in the crystal. There are three jumps in the case of oxygen vacancies, corresponding to the migration of $V_O^{(1)}$, $V_O^{(2)}$, and $V_O^{(3)}$ along the b axis of the crystal. These jumps are denoted as $p1$, $p2$, and $p3$ respectively. Similarly, in the case of gallium vacancies there are two such jumps corresponding to $V_{Ga}^{(1)}$ and $V_{Ga}^{(2)}$, denoted as $q1$ and $q2$ respectively. Because these jumps are along a path with only one component parallel to the b axis of the crystal, they are omitted from Fig. 4 for simplicity. The metastable sites of $V_{Ga}^{(b)}$ and $V_{Ga}^{(c)}$ divide the corresponding paths into two equivalent $q9$ and $q7$ jumps respectively. On the other hand, $V_{Ga}^{(a)}$ divides the path into two nonequivalent jumps denoted as $q4$ and $q5$.

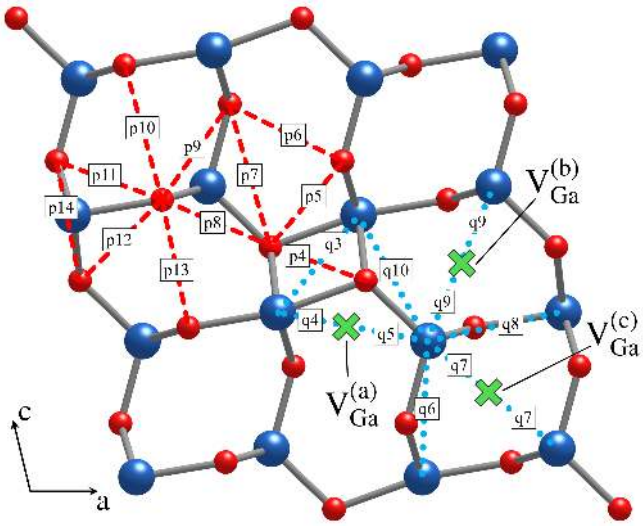

FIG. 4. The possible migration paths of the oxygen (p) and gallium (q) vacancies in the crystal structure of β-Ga_2O_3. The crossmarks designate the positions of the metastable sites of the gallium vacancies.

As mentioned before, there are three different oxygen atoms and two different gallium atoms in the crystal. Therefore, in most cases the initial and final states are different. For instance, jump $p5$ refers to the migration of an oxygen vacancy between an $O^{(1)}$ and an $O^{(3)}$ site. As a result, the direction of the reaction is important in defining the migration barrier. By convention, we define the migration barrier in such cases as the energy difference of the saddle point and the lowest energy state. Hence, we always consider the direction which exhibits the highest barrier between the two.

In the case of the formation energies calculations, supercells of more than 160 atoms yield converged results. In fact, even the smaller supercell of 120 atoms yields formation energies that are in good agreement with the converged values. However, in the case of migration barriers, the 120-atom supercell is insufficient to produce good results. Even the 160-atom supercell produces results that are in good agreement with the converged values only for a few migration paths. We attribute this behavior to the elastic interactions due to the large local deformations caused by the migrating species at the saddle point. This indicates the importance of considering the elastic interactions corrections when calculating migration barriers in small size supercells. Supercells of up to 360 atoms were employed for determining the convergence of the migration barriers. The $1/L^3$ scaling to the infinite size supercell was also considered. Most of our calculated migration barriers were unaffected by the extrapolation to the infinite size supercell due to the already large size of the supercells used. Only very few migration barriers such as $p3$ and $p6$ were affected by the elastic corrections. Even in these extreme cases, the elastic correction affected the calculated values obtained by our largest supercell by less than 0.1 eV. Table I summarizes our results for the migration barriers of both the oxygen and the gallium vacancies in all the charge states and paths.

Based on our formation energies calculations, oxygen vacancies are more likely to occur in the +2 charge state while gallium vacancies most likely occur in the −3 charge state. These charge states also exhibit the lowest migration barriers among the oxygen and gallium vacancies respectively. Moreover, gallium vacancies exhibit significantly lower migration barriers compared to oxygen vacancies. More specifically, the median value of the migration barriers for V_O^{2+} and V_O^0 is 1.8 eV and 2.6 eV respectively. On the other hand, only a small fraction of gallium vacancy jumps exhibit barriers above 2 eV. Most of them are below 2 eV and in some cases they are even lower than 1 eV. These results indicate that gallium vacancies are mobile at much lower temperatures compared to the oxygen vacancies. Fig. 5 shows two cases of the calculated migration barriers using the CI-NEB method. It also demonstrates the importance of the metastable sites in the migration of the gallium vacancies. In this particular case, the migrating vacancy needs to overcome a low barrier of 0.3 eV to reach the metastable state $V_{Ga}^{(c)}$. Following the opposite direction, the vacancy would need to overcome a barrier of 1.4 eV. The situation is similar for $V_{Ga}^{(b)}$. This result suggests that gallium vacancies could be trapped in these metastable configurations before they could be annealed.

Metastable sites are usually high symmetry configurations along the migration path. A common way to locate metastable sites is by studying the migration of species using a chain of states method such as the NEB.

TABLE I. The migration barriers of the oxygen and gallium vacancies in all the charge states and migration paths for β-Ga_2O_3.

Jump (V_O)	Barrier (eV)		Jump (V_{Ga})	Barrier (eV)			
	$q=+2$	$q=0$		$q=0$	$q=-1$	$q=-2$	$q=-3$
p1	1.9	2.2	q1	0.9	1.0	1.0	0.9
p2	2.4	4.0	q2	1.4	1.4	1.2	1.0
p3	1.2	1.7	q3	2.3	2.3	2.3	2.2
p4	1.6	2.6	q4	1.0	0.9	0.7	0.6
p5	1.7	2.2	q5	0.7	0.5	0.6	0.7
p6	1.4	2.0	q6	1.7	1.5	1.2	1.1
p7	2.7	3.3	q7	0.7	0.8	1.0	1.4
p8	1.9	2.9	q8	2.1	1.8	1.7	1.8
p9	1.6	2.6	q9	1.0	1.1	1.0	1.0
p10	2.5	3.1	q10	1.8	1.6	1.6	1.8
p11	1.6	2.5					
p12	1.9	2.6					
p13	1.9	2.6					
p14	1.6	2.5					

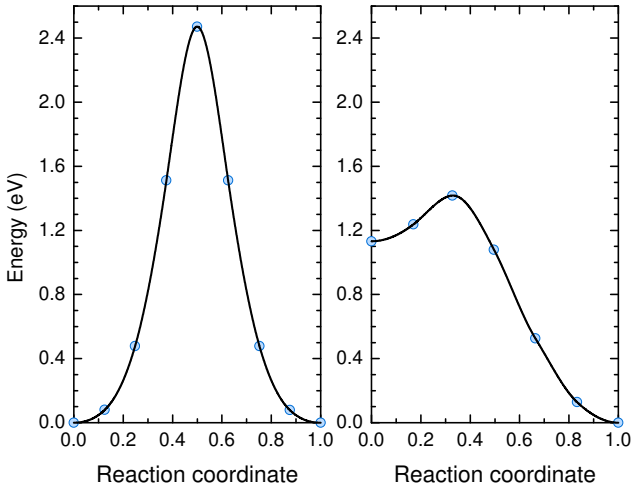

FIG. 5. Migration barrier of the V_O^{2+} for the jump $p10$ (left) and V_{Ga}^{3-} for the jump $q7$ (right) obtained by CI-NEB calculations using nine and seven images respectively.

Apart from jumps $p10$ and $p13$ where the oxygen atom at the saddle point adopts an octahedral configuration with the surrounding atoms, there are no other high symmetry sites along the migration paths of oxygen vacancies. On the contrary, there is a number of high symmetry sites along the migration paths of the gallium vacancies. Jumps $q1$, $q2$, and $q3$ are the only ones which do not involve passing from a high symmetry site. In these sites the migrating gallium atom adopts either a tetrahedral or an octahedral configuration with the surrounding oxygens. More specifically, in the case of $q7$ and $q9$ the high symmetry site along the migration path adopts an octahedral configuration while a tetrahedral configuration is adopted in all the rest. Both octahedral sites along $q7$ and $q9$, i.e., $V_{Ga}^{(b)}$ and $V_{Ga}^{(c)}$, are metastables and they are essential in the migration of gallium vacancies as demonstrated also in Fig. 5. The only tetrahedral site along the migration paths of gallium vacancies with a significant role is the metastable site denoted as $V_{Ga}^{(a)}$ which separates jumps $q4$ and $q5$. The rest of the high symmetry sites along the migration paths were not observed to exhibit local minima properties, hence they could not act as traps for the migrating atom.

IV. DISCUSSION

Using the calculated migration barriers, one can estimate the defect annealing temperatures. A defect becomes mobile and is able to be annealed once it acquires enough energy to overcome the migration barrier. According to the harmonic transition state theory (HTST), the vibrational modes at the stable sites of the atoms, as well as the modes perpendicular to the reaction coordinate at the saddle point are considered to be harmonic. Using HTST, the rate of a reaction, e.g., a migration process, is given as[53]

$$\Gamma = \Gamma_0 e^{-\frac{E_b}{k_B T}}, \tag{6}$$

where E_b is the migration barrier of the given reaction, k_B is the Boltzmann constant, T is the temperature, and Γ_0 is a prefactor commonly known as the attempt frequency. In a more rigorous approach, the prefactor Γ_0 is calculated as the product of the vibrational frequencies at the stable site over the product of the vibrational frequencies at the saddle point. A detailed calculation of the prefactor is beyond the scope of this work, but the value of a typical phonon frequency can be used as a good approximation instead. Hence, solving Eq. (6) with respect to temperature and using $\Gamma = 1\,\text{Hz}$, $\Gamma_0 = 10^{13}\,\text{Hz}$, and the calculated migration barriers we can estimate the temperatures at which the defects become mobile. Fig. 6 shows a graphical representation of the results presented in Table I along with the estimated annealing temperatures.

Typical experimental annealing temperatures of Ga_2O_3 samples fall in the range of 800–1000 °C which is in excellent agreement with our calculations.[6,54–57] In the previous work of Blanco *et al.*, the authors reported values as low as 0.5 eV and 0.1 eV for the migration barriers of oxygen and gallium vacancies respectively. Additionally, they used the interatomic potentials approach considering only neutral defects. Our calculations for the neutral defects suggest minimum barriers of 1.7 eV and 0.7 eV for V_O^0 and V_{Ga}^0 respectively. We attribute this large difference in the classical method used by Blanco *et al.*, which fails to capture many aspects of the migration process such as the complex potential energy surface that develops during the migration of the species. Such low barriers also fail to explain the much higher annealing temperatures observed in Ga_2O_3.

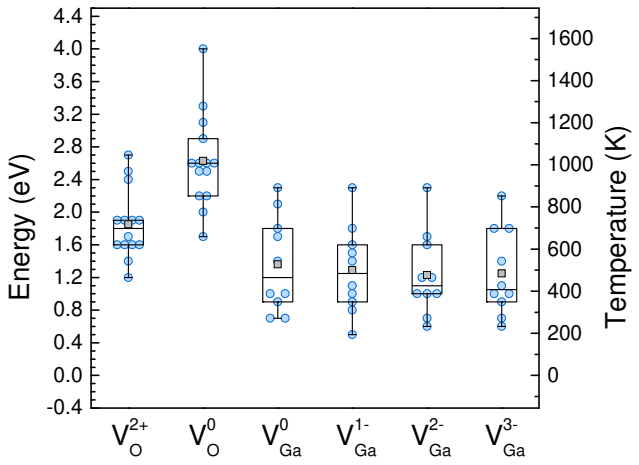

FIG. 6. The migration barriers of the oxygen and gallium vacancies in β-Ga_2O_3 in all the charge states. The left axis represents the energy of the migration barrier and the right axis shows the corresponding annealing temperature based on Eq. (6).

It is evident from Fig. 6 that the gallium vacancies are mobile at much lower temperatures compared to the oxygen vacancies. The fact that gallium vacancies exhibit lower migration barriers might seem counterintuitive since gallium is a larger atom. However, similar results have been observed in other cases such as GaN[50] and ZnO[58] where gallium and zinc vacancies exhibit lower migration barriers than nitrogen and oxygen vacancies respectively. Additionally, the lowest migration barriers for the native defects in GaN have been observed for gallium interstitials which is indicative for the mobility of Ga atoms.[50]

At high enough temperatures, all the paths contribute to the migration of the species through the vacancy mechanism. However, the migration barriers of different paths of gallium and oxygen vacancies at a given charge state may vary by more than 1.5 eV, as seen in Fig. 6. This indicates that even though the lowest in energy path might be active, the highest in energy path might require another 600 K to become relevant. Hence, a question that arises is whether annealing is possible at lower temperatures where some of the paths are either not favored or there is not enough thermal energy to overcome the migration barrier. To answer this, let us use as an example the migration of an oxygen vacancy in the +2 charge state. To help illustrate the answer we will employ some terminology from the field of network science. One may consider the lattice constructed by the available paths as a network in which the nodes represent the atomic sites and the edges represent the paths connecting those sites. Accordingly, percolation occurs once a giant component is formed in the network. A network containing a giant component is said to percolate and the point at which the percolation transition occurs is called the percolation threshold.[59] The giant component in this case will form once there are enough edges on the network so that all the possible atomic sites are be connected. In other words, any atomic site can be reached following a certain set of migration paths. In the case of oxygen vacancies we identified 14 different paths. Sorting them in terms of ascending migration barrier and considering only the first six, a giant component is formed, allowing for diffusion in any direction of the crystal. Fig. 7 illustrates the network of available sites for the migration of the oxygen vacancy. The giant component which arises and connects all the available sites is shown with bold edges. As a result, the plethora of different paths in the monoclinic Ga_2O_3 enables a species to use alternative routes even at low temperatures. In fact, some of the paths are redundant for the migration towards a certain direction and only a certain number of them is required.

As a final remark, we would like to mention that the calculated migration barriers refer to thermal diffusion. In other words, no external mechanisms assist the migration. However, under certain conditions, the barriers might change significantly. For instance, migration of charged defects may be enhanced by the application of an external electric field $\mathcal{E}$ in the direction of the migration. Assuming that q is the charge of the defect and l is the distance between the initial state and the saddle point, the barrier lowering is given by[60]

$$\Delta E = \mathcal{E} q l. \tag{7}$$

A typical jump distance is of the order of a few angstroms and a typical electric field for devices is of the order of 5 MV/cm. Under these conditions the barrier lowering of a doubly charged defect is approximately 0.2 eV. Another example is optical excitation which is also known to significantly enhance the migration of point defects[61,62] in a process known as recombination-enhanced migration.[63] The most commonly discussed mechanism for this process is when the optical excitation results in the non-radiative release of vibrational energy in the vicinity of the defect which assists the defect to overcome its migration barrier. Wide band gap semiconductors with deep trap levels are favored by such a mechanism since the energy converted to vibrational en-

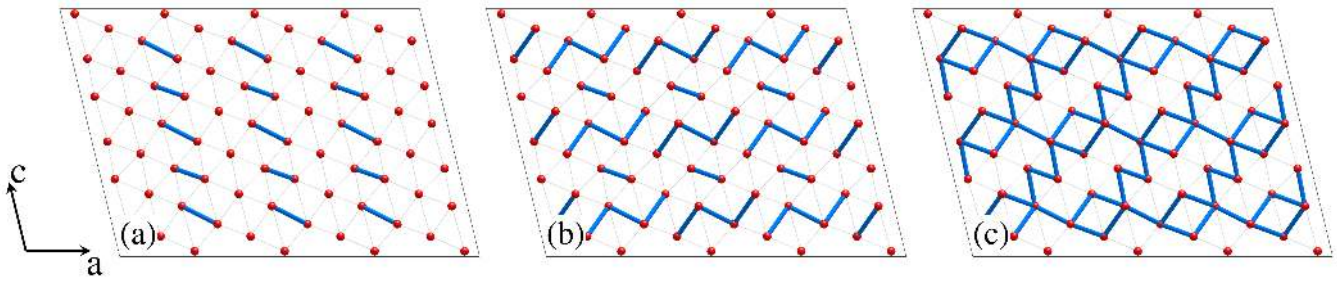

FIG. 7. The sublattice of the oxygen atoms with all the available paths. At low temperatures, (a) and (b), the available paths create small local clusters. Above a certain threshold, (c), a giant component arises and the defects can reach any oxygen site throughout the crystal.

ergy is comparable to the migration barrier.[64] Both oxygen and gallium vacancies introduce deep trap levels in Ga_2O_3. As a result, this mechanism is expected to assist the migration process of the vacancies.

V. CONCLUSION

To summarize, oxygen and gallium vacancies play a crucial role in explaining the properties of Ga_2O_3 and controlling them bears a significant impact in the performance of devices. We employed the nudged elastic band and the dimer methods to determine the minimum energy paths and the migration barriers of oxygen and gallium vacancies in Ga_2O_3. We performed our calculations within the standard DFT framework.

We examined all the possible charge states of oxygen and gallium vacancies and we identified all the possible first nearest neighbor migration paths in the monoclinic structure of Ga_2O_3. Our migration studies revealed the importance of three metastable sites in the case of V_{Ga}. This metastable sites could actually act as traps for gallium vacancies before they could be annealed. Gallium vacancies exhibit significantly lower migration barriers compared to the oxygen vacancies. Their barriers range from 0.5 to 2.3 eV depending on the migration path and the charge state. On the other hand, the barriers for the migration of oxygen vacancies range from 1.2 to 4.0 eV. The abundance of different paths creates numerous ways for the vacancies to migrate isotropically throughout the crystal. However, our results indicate that a percolation mechanism is established at lower temperatures, allowing the defects to utilize certain paths and still migrate isotropically throughout the crystal.

Finally, we used the harmonic transition state theory to estimate the annealing temperatures of these defects. Based on our results, the gallium vacancies become mobile at temperatures higher than 500 K. Due to their higher migration barriers, oxygen vacancies require temperatures of more than 1000 K to be annealed which is in excellent agreement with experimental evidence.

ACKNOWLEDGMENTS

The authors gratefully acknowledge financial support from the US Army Research Laboratory through the Collaborative Research Alliance (CRA) Grant No. W911NF-12-2-0023 for Multi-Scale multidisciplinary Modeling of Electronic Materials (MSME). The computational resources were provided by the DoD HPC Open Research Systems and the 2014 Army Research Office DURIP Award Grant No. W911NF-14-1-0432 made to Dr. E. Bellotti.

* Electronic address: akyrtsos@bu.edu

[1] S. Yoshioka, H. Hayashi, A. Kuwabara, F. Oba, K. Matsunaga, and I. Tanaka, Journal of Physics: Condensed Matter **19**, 346211 (2007).
[2] M. Ogita, N. Saika, Y. Nakanishi, and Y. Hatanaka, Applied Surface Science **142**, 188 (1999).
[3] T. Weh, J. Frank, M. Fleischer, and H. Meixner, Sensors and Actuators B: Chemical **78**, 202 (2001).
[4] A. Trinchi, W. Wlodarski, and Y. Li, Sensors and Actuators B: Chemical **100**, 94 (2004).
[5] M. Orita, H. Ohta, M. Hirano, and H. Hosono, Applied Physics Letters **77**, 4166 (2000).
[6] N. Ueda, H. Hosono, R. Waseda, and H. Kawazoe, Applied Physics Letters **70**, 3561 (1997).
[7] H. Ohta, K. Nomura, H. Hiramatsu, K. Ueda, T. Kamiya, M. Hirano, and H. Hosono, Solid-State Electronics **47**, 2261 (2003).
[8] H. Hosono, Thin Solid Films **515**, 6000 (2007).
[9] J. A. Kohn, G. Katz, and J. D. Broder, Am. Mineral **42**, 398 (1957).
[10] S. Geller, The Journal of Chemical Physics **33**, 676 (1960).
[11] K. Yamaguchi, Solid State Communications **131**, 739 (2004).
[12] H. He, R. Orlando, M. A. Blanco, R. Pandey, E. Amzallag, I. Baraille, and M. Rérat, Phys. Rev. B **74**, 195123 (2006).
[13] C. Janowitz, V. Scherer, M. Mohamed, A. Krapf, H. Dwelk, R. Manzke, Z. Galazka, R. Uecker, K. Irmscher, R. Fornari, M. Michling, D. Schmeißer, J. R. Weber, J. B.

Varley, and C. G. V. de Walle, New Journal of Physics **13**, 085014 (2011).
[14] M. Passlack, N. E. J. Hunt, E. F. Schubert, G. J. Zydzik, M. Hong, J. P. Mannaerts, R. L. Opila, and R. J. Fischer, Applied Physics Letters **64**, 2715 (1994).
[15] S. Müller, H. Von Wenckstern, D. Splith, F. Schmidt, and M. Grundmann, physica status solidi (a) **211**, 34 (2014).
[16] E. Aubay and D. Gourier, Physical Review B **47**, 15023 (1993).
[17] L. L. Liu, M. K. Li, D. Q. Yu, J. Zhang, H. Zhang, C. Qian, and Z. Yang, Applied Physics A **98**, 831 (2010).
[18] Q. Feng, J. Liu, Y. Yang, D. Pan, Y. Xing, X. Shi, X. Xia, and H. Liang, Journal of Alloys and Compounds **687**, 964 (2016).
[19] T. Matsumoto, M. Aoki, A. Kinoshita, and T. Aono, Japanese Journal of Applied Physics **13**, 1578 (1974).
[20] J. B. Varley and A. Schleife, Semiconductor Science and Technology **30**, 024010 (2015).
[21] F. Ricci, F. Boschi, A. Baraldi, A. Filippetti, M. Higashiwaki, A. Kuramata, V. Fiorentini, and R. Fornari, Journal of Physics: Condensed Matter **28**, 224005 (2016).
[22] L. Binet and D. Gourier, Journal of Physics and Chemistry of Solids **59**, 1241 (1998).
[23] T. Harwig, F. Kellendonk, and S. Slappendel, Journal of Physics and Chemistry of Solids **39**, 675 (1978).
[24] E. G. Víllora, M. Yamaga, T. Inoue, S. Yabasi, Y. Masui, T. Sugawara, and T. Fukuda, Japanese Journal of Applied Physics **41**, L622 (2002).
[25] T. Onuma, S. Fujioka, T. Yamaguchi, M. Higashiwaki, K. Sasaki, T. Masui, and T. Honda, Applied Physics Letters **103**, 041910 (2013).
[26] T. Harwig and F. Kellendonk, Journal of Solid State Chemistry **24**, 255 (1978).
[27] T. Harwig, G. Wubs, and G. Dirksen, Solid State Communications **18**, 1223 (1976).
[28] J. B. Varley, H. Peelaers, A. Janotti, and C. G. V. de Walle, Journal of Physics: Condensed Matter **23**, 334212 (2011).
[29] T. Zacherle, P. C. Schmidt, and M. Martin, Phys. Rev. B **87**, 235206 (2013).
[30] H. He, M. A. Blanco, and R. Pandey, Applied Physics Letters **88**, 261904 (2006).
[31] B. Liu, M. Gu, and X. Liu, Applied Physics Letters **91**, 172102 (2007).
[32] J. B. Varley, J. R. Weber, A. Janotti, and C. G. Van De Walle, Applied Physics Letters **97**, 142106 (2010).
[33] J. B. Varley, A. Janotti, C. Franchini, and C. G. Van de Walle, Phys. Rev. B **85**, 081109 (2012).
[34] M. Mohamed, C. Janowitz, I. Unger, R. Manzke, Z. Galazka, R. Uecker, R. Fornari, J. R. Weber, J. B. Varley, and C. G. Van De Walle, Applied Physics Letters **97**, 211903 (2010).
[35] M. A. Blanco, M. B. Sahariah, H. Jiang, A. Costales, and R. Pandey, Phys. Rev. B **72**, 184103 (2005).
[36] P. Hohenberg and W. Kohn, Phys. Rev. **136**, B864 (1964).
[37] W. Kohn and L. J. Sham, Phys. Rev. **140**, A1133 (1965).
[38] P. E. Blöchl, Phys. Rev. B **50**, 17953 (1994).
[39] G. Kresse and D. Joubert, Phys. Rev. B **59**, 1758 (1999).
[40] G. Kresse and J. Furthmüller, Phys. Rev. B **54**, 11169 (1996).
[41] J. P. Perdew, K. Burke, and M. Ernzerhof, Phys. Rev. Lett. **77**, 3865 (1996).
[42] H. Jónsson, G. Mills, and K. W. Jacobsen, in *Classical and Quantum Dynamics in Condensed Phase Simulations*, edited by B. J. Berne, G. Ciccotti, and D. F. Coker (World Scientific, 1998) Chap. 16, pp. 385–404.
[43] G. Henkelman and H. Jónsson, The Journal of Chemical Physics **113**, 9978 (2000).
[44] G. Henkelman, B. P. Uberuaga, and H. Jónsson, Journal of Chemical Physics **113**, 9901 (2000).
[45] G. Henkelman and H. Jónsson, The Journal of Chemical Physics **111**, 7010 (1999).
[46] The Transition State Tools implementation for VASP can be obtained from http://theory.cm.utexas.edu/vtsttools.
[47] J. Åhman, G. Svensson, and J. Albertsson, Acta Crystallographica Section C **52**, 1336 (1996).
[48] C. G. Van De Walle and J. Neugebauer, Journal of Applied Physics **95**, 3851 (2004).
[49] C. Freysoldt, J. Neugebauer, and C. G. Van de Walle, Phys. Rev. Lett. **102**, 016402 (2009).
[50] A. Kyrtsos, M. Matsubara, and E. Bellotti, Phys. Rev. B **93**, 245201 (2016).
[51] C. Freysoldt, B. Grabowski, T. Hickel, J. Neugebauer, G. Kresse, A. Janotti, and C. G. Van de Walle, Rev. Mod. Phys. **86**, 253 (2014).
[52] D. Sheppard and G. Henkelman, J. Comput. Chem. **32**, 1769 (2011).
[53] G. H. Vineyard, Journal of Physics and Chemistry of Solids **3**, 121 (1957).
[54] G. Wagner, M. Baldini, D. Gogova, M. Schmidbauer, R. Schewski, M. Albrecht, Z. Galazka, D. Klimm, and R. Fornari, physica status solidi (a) **211**, 27 (2014).
[55] D. Y. Guo, Z. P. Wu, Y. H. An, X. C. Guo, X. L. Chu, C. L. Sun, L. H. Li, P. G. Li, and W. H. Tang, Applied Physics Letters **105**, 023507 (2014).
[56] M. Baldini, M. Albrecht, A. Fiedler, K. Irmscher, D. Klimm, R. Schewski, and G. Wagner, Journal of Materials Science **51**, 3650 (2016).
[57] Y. Zhang, J. Yan, Q. Li, C. Qu, L. Zhang, and W. Xie, Materials Science and Engineering: B **176**, 846 (2011).
[58] A. Janotti and C. G. Van de Walle, Phys. Rev. B **76**, 165202 (2007).
[59] M. E. J. Newman, *Networks: An Introduction* (Oxford University Press, Inc., New York, NY, USA, 2010).
[60] K. H. Warnick, Y. Puzyrev, T. Roy, D. M. Fleetwood, R. D. Schrimpf, and S. T. Pantelides, Phys. Rev. B **84**, 214109 (2011).
[61] P. Johannesen, A. Zakrzewski, L. S. Vlasenko, G. D. Watkins, A. Usui, H. Sunakawa, and M. Mizuta, Phys. Rev. B **69**, 045208 (2004).
[62] K. H. Chow and G. D. Watkins, Phys. Rev. Lett. **81**, 2084 (1998).
[63] L. Kimerling, Solid-State Electronics **21**, 1391 (1978).
[64] J. D. Weeks, J. C. Tully, and L. C. Kimerling, Phys. Rev. B **12**, 3286 (1975).